GEOPHYSICS

Metamorphic records of multiple seismic cycles during subduction

Daniel R. Viete,[1]* Bradley R. Hacker,[2] Mark B. Allen,[3] Gareth G. E. Seward,[2] Mark J. Tobin,[4] Chris S. Kelley,[5] Gianfelice Cinque,[5] Andrew R. Duckworth[6]

Large earthquakes occur in rocks undergoing high-pressure/low-temperature metamorphism during subduction. Rhythmic major-element zoning in garnet is a common product of such metamorphism, and one that must record a fundamental subduction process. We argue that rhythmic major-element zoning in subduction zone garnets from the Franciscan Complex, California, developed in response to growth-dissolution cycles driven by pressure pulses. Using electron probe microanalysis and novel techniques in Raman and synchrotron Fourier transform infrared microspectroscopy, we demonstrate that at least four such pressure pulses, of magnitude 100–350 MPa, occurred over less than 300,000 years. These pressure magnitude and time scale constraints are most consistent with the garnet zoning having resulted from periodic overpressure development-dissipation cycles, related to pore-fluid pressure fluctuations linked to earthquake cycles. This study demonstrates that some metamorphic reactions can track individual earthquake cycles and thereby opens new avenues to the study of seismicity.

INTRODUCTION

Earthquakes in subduction zones can produce devastating tsunamis [for example, the 2004 moment magnitude (M_w) 9.2 Sumatra-Andaman and 2011 M_w 9.0 Tōhoku "megathrust" earthquakes] and may discharge subducted volatiles (*1*, *2*) and trigger arc magmatism (*3*, *4*). Although subduction seismicity can persist to depths of >600 km, it is most frequent and energetic in the uppermost part of the subducting slab, at depths of 30 to 70 km (*5*–*8*). The record of such seismicity might be visible in high-pressure/low-temperature (H*P*/L*T*) metamorphic rocks recovered from these depths. More so than for other tectonic environments, links between metamorphism and seismicity are proposed for subduction zones. For example, seismicity at anomalous (>50 to 70 km) depths in the subduction setting has been related to embrittlement due to metamorphic dehydration reactions and associated pore fluid pressure development and/or volume change (*6*, *9*–*14*). Geologic records that contribute to our understanding of the mechanisms and magnitude recurrence rates for subduction seismicity come chiefly from Quaternary tsunami and turbidite deposits (*15*–*20*), subsidence/uplift histories from tidal wetlands and coral reefs (*21*, *22*), and pseudotachylytes and breccias (*23*–*25*). Here, we show that garnet—one of the more common metamorphic minerals in H*P*/L*T* metamorphic rocks—may provide new insights into earthquake magnitude recurrence rates.

The blueschist- and eclogite-facies assemblages produced in subduction metamorphism record uniquely low geothermal gradients, typically <600°C GPa^{-1}. Subduction metamorphism can be incredibly rapid, in cases involving time scales <10^4 to 10^6 years (*26*–*29*). Rhythmic major-element zoning in garnet is a common feature in H*P*/L*T* metabasic rocks (*30*–*36*), suggesting that it is a manifestation of a common process (or set of processes) in the subduction setting. To explore the nature of these processes and the origin of the H*P*/L*T* garnet zoning, we apply several modern and novel techniques to investigate metamorphism and paleoseismicity in the Jurassic Franciscan Complex, California.

RESULTS

Sample CA13-01 is a garnet-bearing eclogite-blueschist from Ring Mountain, Tiburon Peninsula, San Francisco Bay. Sample CA13-05A is a garnet-rich amphibolite from the same locality. Detailed rock descriptions are provided in Materials and Methods; however, of particular relevance for the *P*-*T* conditions of metamorphism is the presence of amphibole (glaucophane in CA13-01; Na-Ca amphibole and glaucophane in CA13-05A) and zoisite and the absence of lawsonite in both samples. Garnets from both rocks contain rutile and quartz inclusions from the core to the rim (with quartz being rare at the rim). Thermodynamic modeling of phase equilibria suggests that garnet rim growth occurred under *P*-*T* conditions of 555° to 585°C and 1.4 to 2.0 GPa for CA13-01 and 535° to 595°C and 1.2 to 2.0 GPa for CA13-05A; these estimates are entirely consistent with earlier thermobarometry of the same rocks (*37*). Whole-rock geochemistry, methods, and results for thermodynamic modeling of metamorphic phase equilibria are provided in Materials and Methods.

Electron microprobe x-ray count maps were produced for Ca, Fe, Mg, and Mn in six to seven garnets for each of CA13-01 and CA13-05A; examples of Mg and Mn maps are provided in Fig. 1, and all maps are provided in the Supplementary Materials. Complementary quantitative electron microprobe traverses were measured for one garnet from CA13-01 and two garnets from CA13-05A (Fig. 1). The garnets have inclusion-rich cores that are compositionally distinct from inclusion-poor mantles/rims (Fig. 1). Oscillatory/rhythmic zoning in both Mg and Mn is apparent in the mantle/rim zone (Fig. 1) but does not correspond to obvious zoning in Ca or Fe (with the exception of bands at the extreme outer edge of garnets from CA13-01). The Mg and Mn zoning in some garnets incorporates features of zone incursion (embayments) and circumferential pinching and swelling (Fig. 1). All garnets analyzed display systematic asymmetry in the location of relatively steep compositional gradients (Fig. 1). These features are consistent with the major-element zoning being a result of cycles of garnet growth separated by gaps during which there was no growth or there was dissolution, such that the embayments and steep compositional

[1]Department of Earth & Planetary Sciences, Johns Hopkins University, Baltimore, MD 21218, USA. [2]Department of Earth Science, University of California, Santa Barbara, Santa Barbara, CA 93101, USA. [3]Department of Earth Sciences, Durham University, Durham DH1 3LE, UK. [4]Australian Synchrotron, Clayton, Victoria 3168, Australia. [5]Diamond Light Source, Harwell Science and Innovation Campus, Didcot OX11 0DE, UK. [6]Department of Chemistry, Durham University, Durham DH1 3LE, UK.
*Corresponding author. Email: viete@jhu.edu

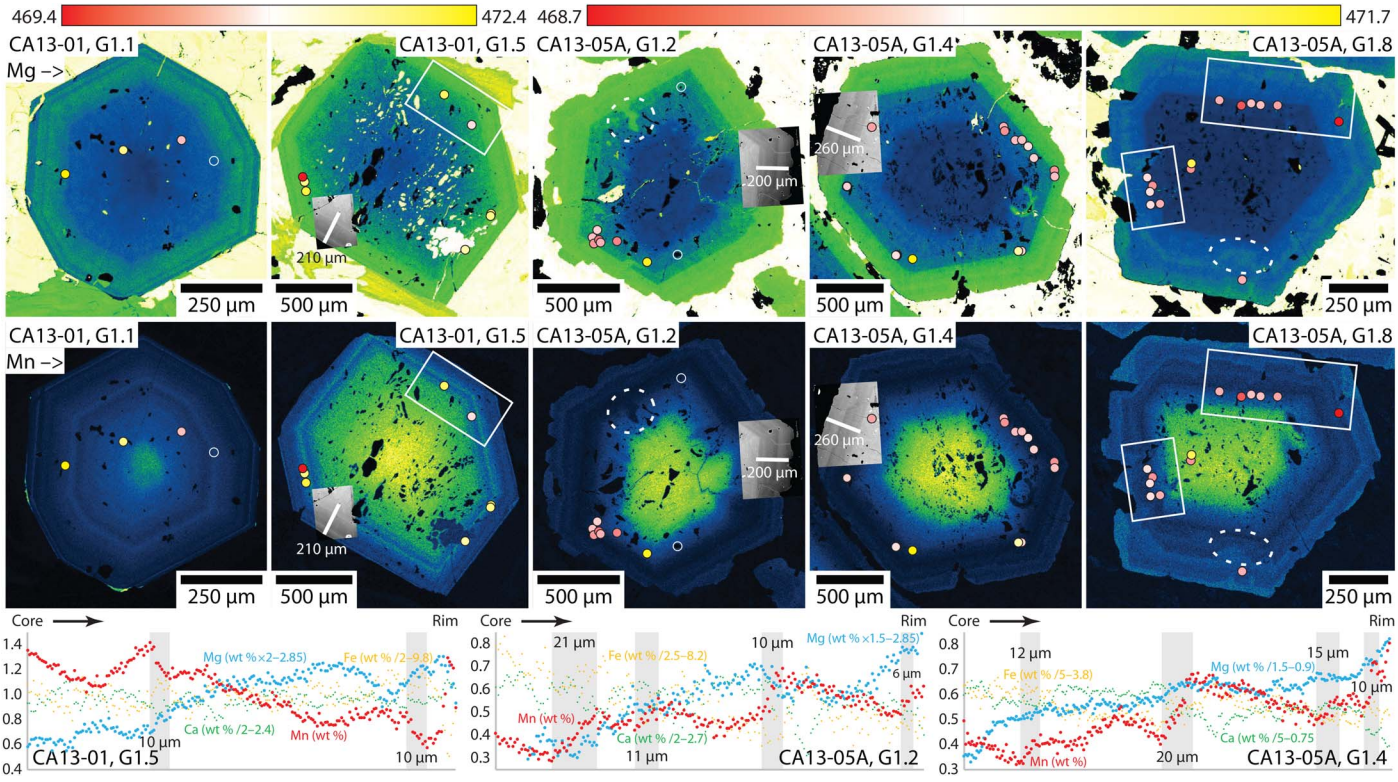

Fig. 1. Garnet compositional maps and profiles. Color-enhanced wavelength-dispersive spectrometer (WDS) x-ray count maps for Mg (top row) and Mn (middle row) in garnets from Ring Mountain. Decreasing Mg and Mn content are indicated by yellow-green-blue-black color progression. Spots give location of Raman quartz analyses and are colored according to peak position (±1.5 cm^{-1} about 470.9 cm^{-1} for CA13-01; ±1.5 cm^{-1} about 470.2 cm^{-1} for CA13-05A; see data in Fig. 3D). Transparent spots correspond to partially transparent analyses in Fig. 3D. Spot size indicated is larger than the actual ~1-µm spot. White rectangles show notable zones with varying Raman response associated with compositional zoning boundaries (blowups provided in the Supplementary Materials). Dashed white ellipses highlight examples of zoning embayments/incursions. Gray backscattered electron (BSE) images indicate locations of quantitative (WDS) electron microprobe traverses at the bottom of the figure. Regions with steep compositional gradients in the traverses are indicated by vertical gray bands (with length scale indicated).

gradients mark garnet growth "unconformities." Quantitative Mn traverses (Fig. 1) confirm the asymmetry in the compositional gradients that flank the Mn highs; relatively steep gradients occur on the rim side of Mn highs for sample CA13-01 and on the core side for sample CA13-05A. Rim-side asymmetry (as observed in CA13-01) must involve overgrowth of thin (high-Mn) resorption bands by lower-Mn garnet, whereas core-side asymmetry (as observed in CA13-05A) must involve overgrowth of the unconformity surface by higher-Mn garnet. The two modes presumably reflect different supply/demand scenarios for Mn following garnet dissolution; reactions associated with the rim-side scenario cannot provide a sanctuary for all Mn liberated by garnet dissolution, leading to back diffusion of Mn into the garnet. Figure 2 outlines models for the development of the two types of asymmetric zoning as a result of garnet growth-dissolution cycles.

Franciscan garnet growth-dissolution cycles due to pressure(-temperature) fluctuations

The modal garnet contours for both rocks (see phase assemblage diagrams in Materials and Methods) suggest that modest changes in T or, more so, P might have triggered significant garnet production/loss and therefore caused the garnet zoning (that is 5 to 15 volume % growth/dissolution, relative to starting garnet content, for a ΔT of 40°C or a ΔP of 100 MPa). The gentle slopes in P-T space for both Mg- and Mn-in-garnet isopleths (see phase assemblage diagrams in Materials and Methods) are also consistent with rhythmic zoning in Mg and Mn having developed primarily in response to changes in P. Garnet zoning is complemented by irregular major-element zoning in glaucophane, omphacite, and zoisite in CA13-01, and glaucophane, hornblende, and zoisite in CA13-05A. Up-pressure dehydration reactions likely involved breakdown of glaucophane and zoisite to form garnet, jadeite, quartz, and H_2O in CA13-01 and breakdown of hornblende and zoisite to form garnet, glaucophane, and H_2O in CA13-05A (see Materials and Methods). To test the role of pressure fluctuations in driving garnet growth-dissolution cycles, we performed high-resolution barometry by Raman microspectroscopy on quartz inclusions in garnet and novel synchrotron Fourier transform infrared (FTIR) microspectroscopy on garnet.

Interrogating pressure pulses by spectroscopic methods

Raman barometry uses the pressure dependence of the position of peaks in the Raman spectra for an included mineral to calculate a residual pressure in the inclusion (*38*). This residual pressure results from differential expansion/contraction of host and inclusion following cooling and exhumation and, knowing the thermoelastic properties of the two minerals, can be used to calculate the P-T conditions of inclusion overgrowth by host. The properties of quartz and garnet yield an inclusion-host system far more sensitive to overgrowth pressure than temperature, meaning that the quartz-in-garnet system makes

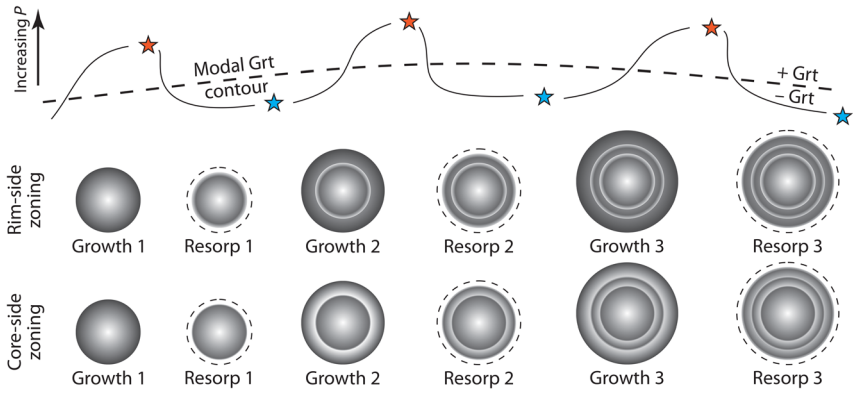

Fig. 2. Model for garnet zoning in response to pressure pulses. Conceptual models for development of rim-side (top row of garnets with Mn back diffusion during resorption) and core-side zoning (bottom row of garnets with no Mn back diffusion during resorption) by fluctuating garnet stability (growth-resorption cycles) in response to pressure pulses. Blue stars mark the onset of undrained conditions at the start of a phase of fluid overpressure development and garnet growth. Orange stars mark full overpressure conditions at the end of a growth phase (immediately before an earthquake event and fracturing due to dynamic stresses and relief of overpressure). Grt, garnet.

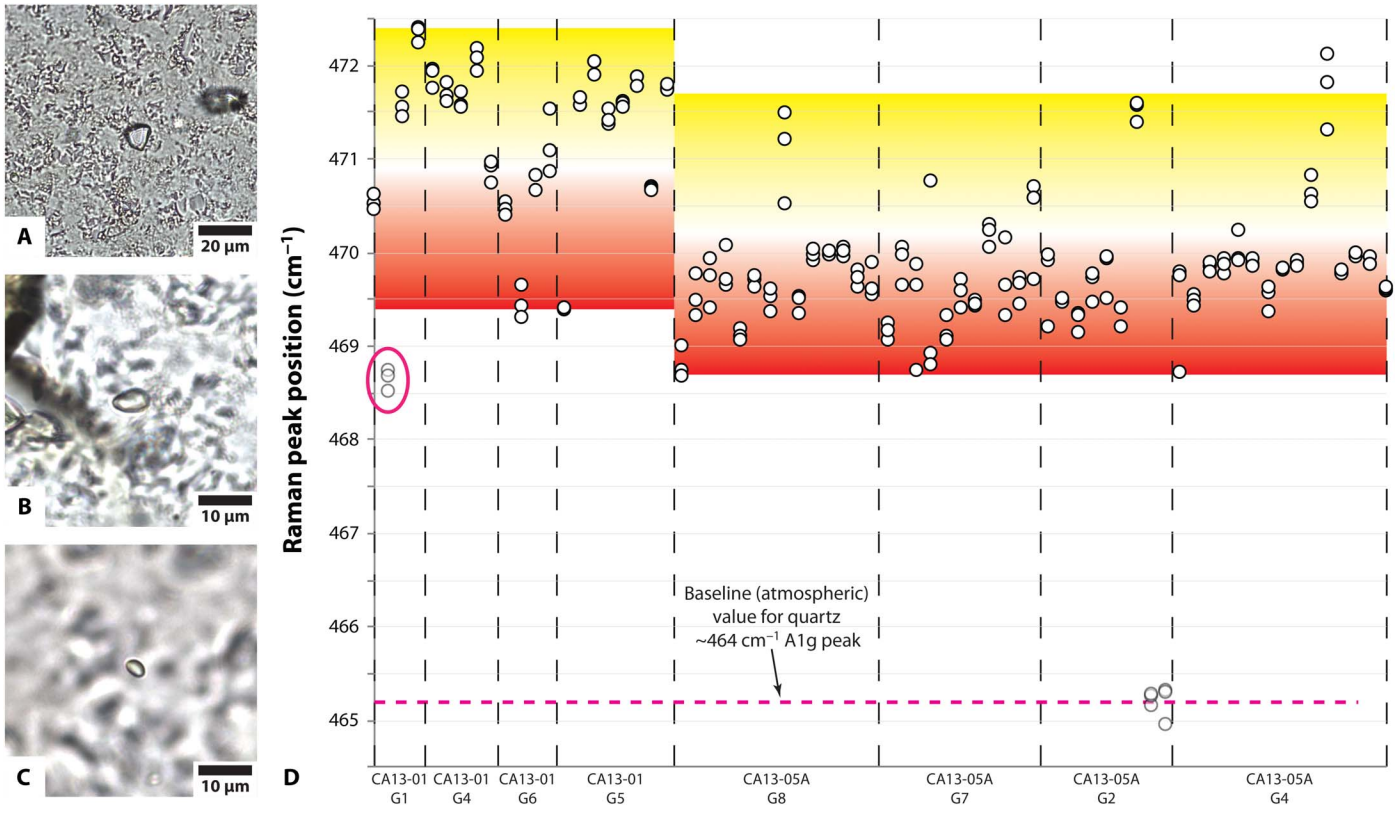

Fig. 3. Quartz-in-garnet Raman microspectroscopy results. (**A** to **C**) Transmitted-light photomicrographs of some analyzed quartz inclusions in garnet. (**D**) Positions for the nominally 464 cm^{-1} A1g Raman peak for quartz inclusions in garnet from Ring Mountain, analyzed in triplicate. Inclusion circled in pink displays an abnormally low peak position despite lack of evidence that it was exposed during polishing or associated with visible cracks in garnet. Yellow-to-red background coloring is shown for reference to spot colors on garnet x-ray count maps in Fig. 1.

a good barometer (*39*). The position of (nominal 464 cm^{-1}) quartz Raman A1g-mode peaks was measured in triplicate for 80 quartz-in-garnet inclusions across samples CA13-01 and CA13-05A. Images of quartz inclusions are provided in Fig. 3 (A to C), and detailed methods are provided in Materials and Methods. Repeat analyses produced consistent results, yielding a 2σ reproducibility of ±0.3 cm^{-1} (Fig. 3D). With exposed, cracked, or compound inclusions (n = 12) excluded, analyses from the two rocks show a significant spread in A1g-mode peak position (4.2 to 7.2 cm^{-1} above atmospheric for CA13-01 and 3.5 to 6.5 cm^{-1} above atmospheric for CA13-05A; Fig. 3D). Variable Raman A1g-mode peak position reflects variable residual pressure resulting from different overgrowth pressure. Using the calibration of Schmidt and Ziemann (*40*), the elastic model of Guiraud and Powell (*41*), and mineral properties recommended by Holland and Powell (*42*), the ranges of Raman A1g-mode peak shifts suggest P = 1.4 to 2.1 GPa (median, 1.9 GPa) for CA13-01 and P = 1.25

to 1.95 GPa (median, 1.5 GPa) for CA13-05A. Spatially, Raman A1g-mode peak position varies by 0.5 to 1.5 cm^{-1} over garnet radial distances of 10 to 50 μm and in association with the major-element growth zoning (Fig. 1); we infer that garnet growth-dissolution cycles were associated with fluctuations in metamorphic pressure of magnitude 100–350 MPa.

Raman barometry can only be applied where suitable inclusions occur. To obtain more complete records of pressure fluctuations during garnet growth/resorption, we also applied exploratory FTIR absorption spectroscopy for simultaneous garnet barometry and hygrometry. Experimental work has demonstrated a positive relationship between growth pressure and the OH content of pyrope garnet [at mantle pressures; (*43*, *44*)], and the presence of nonstructural (molecular) H_2O in garnet (an impurity) may also act as a proxy for the activity (partial pressure) of H_2O (a hygrometer) during garnet growth. Structural OH and molecular H_2O in garnet are associated with independent FTIR spectral peaks within the mid-infrared (IR) range. Interrogation of the fine major-element zoning in the Franciscan *HP/LT* garnets by FTIR spectroscopy requires high–spatial resolution and high-sensitivity measurement of a component that occurs in extremely low concentrations (<100 parts per million; garnet is nominally anhydrous), meaning that the technique requires an IR source with brightness only offered by synchrotron light. Transmission synchrotron FTIR microspectroscopy was performed on three garnets from CA13-01 and two from CA13-05A at the Australian Synchrotron and Diamond Light Source, UK. Detailed methods and results are provided in Materials and Methods.

Our new, qualitative synchrotron FTIR barometry and hygrometry technique identified regions with steep OH (and, to a lesser extent, H_2O) concentration gradients in garnet (Fig. 4). These breaks in OH match the locations of the steep compositional gradients that mark garnet growth unconformities (Fig. 4). The correlation is with

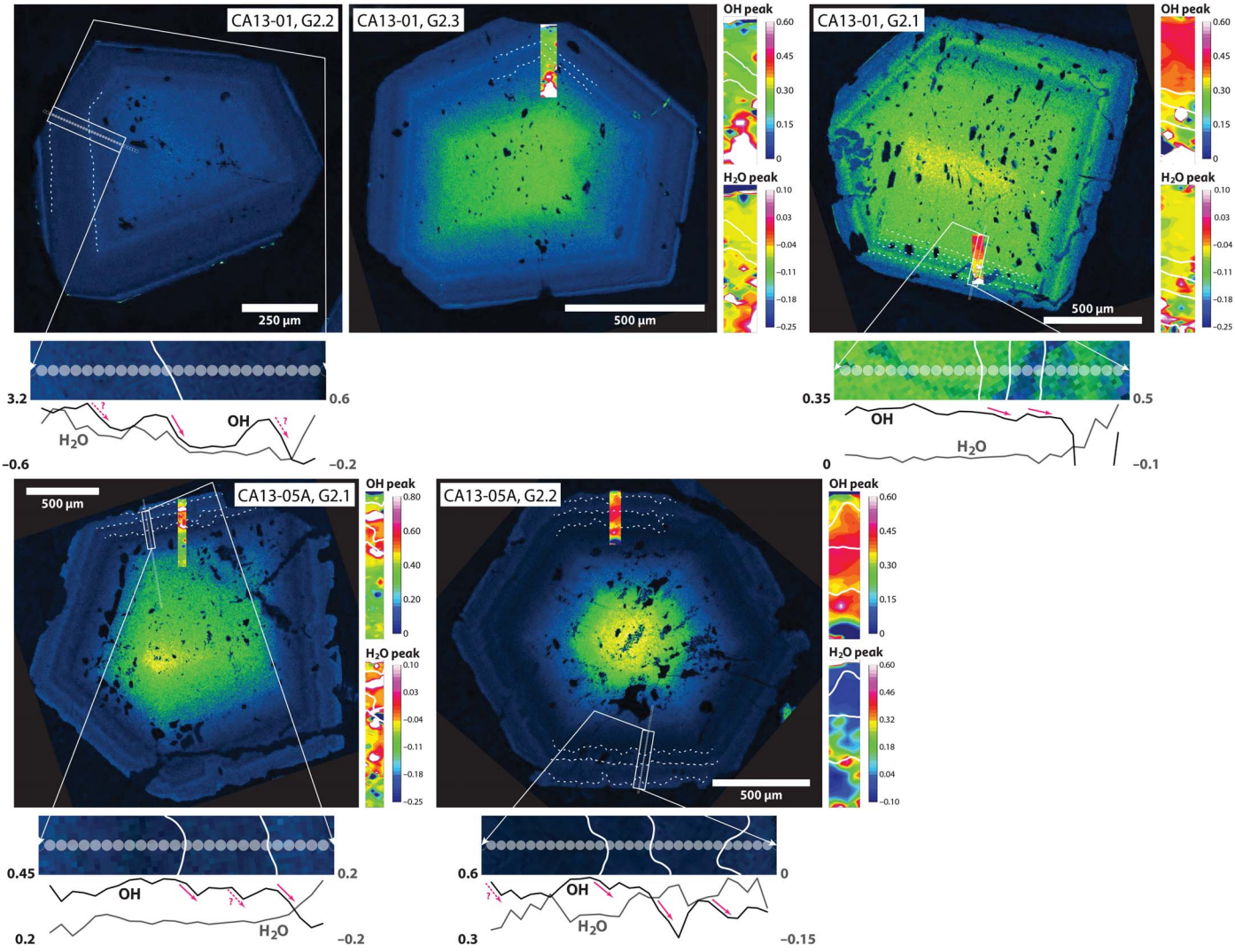

Fig. 4. Synchrotron FTIR microspectroscopy results. X-ray count maps for Mn in garnet and synchrotron FTIR analysis for one-dimensional (1D) traverses (bottom of each Mn map) and two-dimensional (2D) maps (right of each Mn map) for OH and H_2O. Dashed white lines on Mn maps indicate the position of garnet growth unconformities and correspond to the white lines on the 1D FTIR traverses and 2D FTIR maps. Vertical axis on 1D traverse plots and colors of the 2D FTIR maps correspond to integrated intensity in the 3520 to 3620 cm^{-1} region for OH (a dimensionless measure of OH abundance) and in the 3350 to 3450 cm^{-1} region for H_2O (a dimensionless measure of H_2O abundance). Pink arrows on 1D traverse plots indicate regions of decreasing OH in the vicinity of garnet growth unconformities.

zoning in Mg and Mn but not in Ca, suggesting that fluctuations in OH do not simply reflect changes in proportion of the garnet end members that are most commonly hydrated (that is, grossular/andradite). Regardless of the polarity of Mn change across the unconformities in rim-side (CA13-01) and core-side (CA13-05A) zoning, OH content uniformly shows a sharp rim-side decrease (Fig. 4). This result is consistent with garnet growth (following dissolution) resuming at lower pressure than recorded in the garnet immediately core-side of the growth unconformity—that is, the synchrotron FTIR results indicate that dissolution was associated with a pressure drop. The synchrotron FTIR results demonstrate the linkage between pressure fluctuations and growth-dissolution cycles proposed in the model for development of the fine-scale, rhythmic compositional zoning in the garnets (Fig. 2). The relationship between OH and H_2O in the garnets is complex, displaying covariance or anticorrelation in some regions and apparent independence in others. For these rocks, if systematic mechanistic linkages between pressure and fluid activity exist, then the synchrotron FTIR approach was unable to resolve them.

Short time scales for multiple pressure pulses

The presence of rutile and Ca-Na amphibole in CA13-05A constrains peak T = 535° to 595°C at P = 1.2 to 1.8 GPa, and the presence of glaucophane and the absence of chlorite in CA13-01 constrain peak T = 555° to 585°C for P = 1.4 to 1.95 GPa (see metamorphic assemblage diagrams in Materials and Methods). The presence of rutile inclusions at the edge of garnet rims is consistent with garnet zoning having developed during the peak-T phase of the metamorphism (T > 550°C), in agreement with other work on Ring Mountain H*P*/L*T* garnets (*33*) but in contrast to Franciscan H*P*/L*T* garnets with retrograde rims from Healdsburg (*34*, *45*) and Jenner (*46*). The absence of lawsonite in both rocks suggests slightly lower maximum pressure than calculated from Raman barometry (<1.8 to 2.0 GPa versus 1.9 to 2.1 GPa). The counterclockwise *P*-*T* path experienced by these rocks involved relatively isobaric refrigeration after peak *P*-*T*, followed by monotonic cooling during exhumation (*33*, *34*, *47*). Preservation of fine-scale diffusion textures in garnet that developed during the peak-*T*, garnet rim-growth phase of the metamorphism (≤10 μm, Fig. 1) means that there was negligible modification during exhumation, despite evidence for a protracted exhumation (cooling) history (*45*, *48*).

We use an error function approximation to 1D (radial) diffusion [equation of the form $c(x,t) \propto \mathrm{erf}\,(x/\sqrt{4Dt})$, where c, x, t, and D are concentration, position, time, and diffusivity, respectively] to reproduce Mn diffusion length scales associated with the garnet growth unconformities (≤10 μm, Fig. 1) and thereby constrain time scales for formation of the garnet zoning at near-peak metamorphic conditions. This approach assumes an initial step change in Mn concentration associated with the overgrowth/dissolution surface and no cutting effects or spatial homogenization due to spot size; the calculated estimates are therefore significantly biased toward longer durations. The Mn-in-garnet Arrhenius parameters of Chu and Ague (*49*) yield time scales of <300 thousand years (ky) for T > 550°C and P < 2.0 GPa; all the pressure-driven growth-dissolution cycles must have occurred within this time frame. Varying the overgrowth *P*-*T* from 550° to 590°C and from 1.2 to 2.0 GPa expands the estimate range to <30 to 300 ky. Allowing for Mn-in-garnet Arrhenius parameter values between the most diffusive (*50*) and the most retentive (*51*) published expands the range to <0.04 to 1.2 million years (My) (for mean *P*-*T* conditions; T = 570°C, P = 1.6 GPa). This range is compatible with global subduction speeds (*52*), indicating that most subducting crust passes through blueschist-facies conditions in ~1 My.

DISCUSSION

The diffusion length scale data indicate that at least four cycles of pressure fluctuation (of magnitude 100–350 MPa) occurred during H*P*/L*T* metamorphism, with net garnet growth length scales of <100 to 300 μm and metamorphic time scales very likely <<1 My. On the basis of major-element zoning in H*P*/L*T* garnets from Cuba, García-Casco *et al.* (*31*) hypothesized pressure fluctuations of similar magnitude during subduction, relating them to small-scale (physical) exhumation events during prograde metamorphism. The <<1 My time scales for garnet zoning development are significantly shorter than hypothesized time scales for multiple burial-exhumation cycles in H*P*/L*T* rocks that have been related to (i) "yo-yo tectonics," involving (local or regional) switches between shortening and extension (*35*, *53*–*55*); (ii) exhumation-erosion-deposition-subduction cycles (*56*); and (iii) numerically simulated "chaotic" mixing as a result of convection within a putative subduction channel (*57*–*60*). These "lithostatic pressure" models are limited by maximum rates of burial/exhumation; for example, four 7.5-km (mean magnitude, 225 MPa) burial-exhumation cycles at vertical movement rates approximating tectonic plate velocities—that is, 30 mm year^{-1}, as in the subduction convection model of Gerya *et al.* (*58*)—require at least 2 My. It should be noted, however, that modeling of convection within the subduction channel also predicts periodic stalling of particles, more likely yielding time scales of 5 to 10 My per 200- to 500-MPa physical burial-exhumation cycle [for example, see figures 4 and 7 of the study by Gerya *et al.* (*58*)].

Garnet zoning marks seismic cycles during subduction

Figure 5 compares time scales for (i) megathrust earthquake recurrence, (ii) individual *P* pulses recorded in the H*P*/L*T* garnets of this study, and (iii) small-scale physical burial-exhumation cycles, showing that these constraints are most consistent with a seismic cycle origin for the garnet *P* pulse records. We relate rhythmic major-element zoning in the Franciscan garnets to cycles of pore fluid overpressure

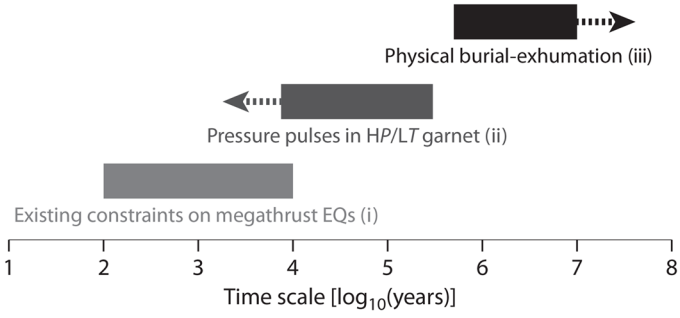

Fig. 5. Time scale comparisons. Time scales for individual cycles relating to (i) megathrust earthquake (EQ) events from tsunami and turbidite deposits and subsidence/uplift histories, (ii) garnet dissolution-growth cycles and associated *P* pulses as recorded in the garnets of this study, and (iii) physical burial-exhumation cycles relating to "yo-yo" tectonics, exhumation-erosion-deposition-subduction cycles, or convection within a putative subduction channel. Note that time scales for (ii) are maximum values due to bias toward overestimation in the approach used and the possibility that *P* pulses were significantly more numerous than recorded in the garnets (see text).

development and dissipation, linked to a seismically induced switch from locally undrained to drained conditions [that is, dynamic cracking and permeability changes following large earthquakes; see the works of Brenguier *et al.* (*61*) and Chaves and Schwartz (*62*)].

Although rocks do not typically have unconfined strength greater than 100 to 200 MPa, the effects of confinement and undrained conditions may allow pore fluid pressure excess (overpressure) to attain more significant values (*63*–*65*). Transient pressure pulses may mark porosity waves that transit the rock volume or cycles of overpressure development-dissipation linked to subduction zone seismicity. Porosity waves are only theorized to exist, whereas subduction zone seismicity is an observed phenomenon that has been associated with pore fluid overpressure (*6*, *9*–*12*) and occurs at the depth and location of H*P*/L*T* metamorphism.

Our model for Franciscan garnet zoning invokes widespread rock fracture with passing seismic waves as the trigger for overpressure relief; changes in seismic velocity following megathrust earthquakes have been related to this mechanism of pore fluid pressure relief (*61*, *62*). Rock fracture in response to dynamic stresses induced by a large earthquake may also produce a widespread permeability spike. Once fault healing and sealing are complete and conditions again become undrained, feedback between dehydration reactions and increasing metamorphic pressure—due to metamorphic pore fluid production—can lead to overpressure development and recommenced garnet growth, until dynamic stresses associated with a subsequent large earthquake again cause rock fracture and permeability increase. Not all earthquake events need be recorded, and those that were need not have been proximal; dynamic stresses and therefore likelihood of local fracturing and overpressure relief would be greatest for the most energetic events (for example, megathrusts). The model is consistent with our FTIR observation of a decrease in OH across the growth unconformity (Fig. 4). Intimate garnet growth zone $\delta^{18}O$ variation in the Franciscan garnets [cf. Page *et al.* (*45*)] may also be expected for cycles of pore fluid purging with rock fracture, pressure drop, and permeability increase, followed by metamorphic dehydration and overpressure development under undrained conditions. Such work may offer a means to test the fluid overpressure relief (following large earthquakes) model presented here.

Multiple, rapid pressure fluctuations of 100 to 350 MPa, as observed here in association with garnet zoning, can be achieved by seismic cycles in subduction zones. Large earthquakes have recurrence intervals of 100 to 10,000 years (*16*–*21*). Although there is some overlap, the H*P*/L*T* garnets studied record frequencies mostly outside of this recurrence range (see Fig. 5). Not every earthquake will cause fracturing and overpressure dissipation; records are only made for those that produced sufficient seismic energy, directed at the rock volume. This, partnered with the potential for garnet dissolution to have removed evidence of earlier garnet growth-dissolution cycles (cannibalization of records of *P* pulses), can explain much of the potential discrepancy between time scales for H*P*/L*T* garnet records of *P* pulses and recurrence intervals for large subduction zone earthquakes (Fig. 5).

We conclude that major-element zoning in the H*P*/L*T* garnets records seismic cycles within the Franciscan subduction zone. These metamorphic features are common in H*P*/L*T* metamorphic rocks worldwide. In time, geochemical features of H*P*/L*T* garnets (and other minerals) may offer important new insights into the nature of subduction zone (paleo)seismicity and associations among stress evolution, earthquake magnitude and recurrence, and fluid transport/mobility in the crust.

MATERIALS AND METHODS

Sample descriptions

The article focuses on two rocks from Ring Mountain, San Francisco Bay, California. Sample CA13-01 [Global Positioning System (GPS): 37°55.073′ N, 122°29.583′ W] is an eclogite-blueschist with 11 volume % garnet. Sample CA13-05A (GPS: 37°54.729′ N, 122°29.122′ W) is a garnet-rich (32 volume %) amphibolite-blueschist. Garnet populations in both rocks are not uniform, with grain size in each varying from <0.5 mm to approximately 2 mm across. Both rocks are heterogeneous on a scale of 1 to 10 mm; CA13-01 has blueschist and eclogite layers, and CA13-05A has interfingered amphibolite and blueschist domains. Garnet in CA13-01 is commonly surrounded by phengite, whereas many garnets in CA13-05A are surrounded by clots of chlorite. Mineralogy for each sample is given below. Cross-polarized light microphotographs are provided in Fig. 6.

(CA13-01) omphacite + garnet + glaucophane + phengite + titanite + zoisite + quartz + rutile

(CA13-05A) hornblende + garnet + glaucophane + zoisite + chlorite + rutile + phengite + omphacite + titanite

Tsujimori *et al.* (*33*) provided detailed descriptions of three H*P*/L*T* rocks from Ring Mountain. Their sample A is incredibly similar in mineralogy and appearance to our CA13-05A. For that sample, Tsujimori *et al.* (*33*) used petrography, garnet-omphacite-phengite thermobarometry, and equilibrium phase assemblage modeling to constrain garnet rim growth to the peak metamorphic phase, at T = 550° to 620°C and P = 2.2 to 2.5 GPa. Titanite overgrew rutile in both CA13-01 and CA13-05A, and chlorite overgrew garnet in CA13-05A. The Ring Mountain H*P*/L*T* rocks record a counterclockwise *P*-*T* path, with a metamorphic overprint relating to refrigeration before exhumation (*33*, *47*). Chlorite and titanite in CA13-01 and titanite in CA13-05A are texturally post-peak metamorphic and grew during the exhumation (and refrigeration) phase of the rock history.

Electron microprobe methods, mineral chemistry and zoning, and Mn sources

Electron microprobe mapping method and results

WDS x-ray count maps for Al, Ca, Fe, Mg, and Mn were produced for seven garnets from CA13-01 and six garnets from CA13-05A. Measurements were made simultaneously on the five spectrometers of the Cameca SX 100 electron microprobe in the Department of Earth Science, University of California, Santa Barbara; Al, Ca, Fe, Mg, and Mn measurements were made on TAP, LPET, LLIF, LTAP, and LLIFF crystals, respectively. Run conditions were 15 keV and 200 nA, and

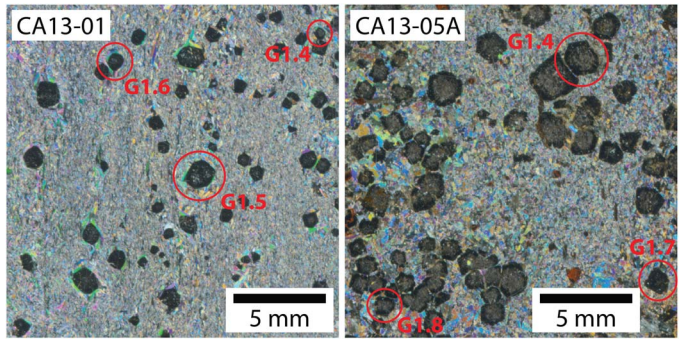

Fig. 6. Cross-polarized-light photomicrographs of samples CA13-01 and CA13-05A. For each rock, some of the garnets mapped for major elements are circled in red.

pixel dwell times were 50 ms for all maps except for CA13-01 garnet 2.3, which used 100 ms. Mapping resolution was 2 to 5 μm, depending on the size of the garnet, and uniform in *x* and y. Color overlay maps for all garnets are provided in the Supplementary Materials.

Electron microprobe quantitative analysis method and results

Quantitative WDS analyses were produced for three radial garnet traverses (n = 670), a cluster of zoned zoisites from each of CA13-01 and CA13-05A (n = 24), and selected additional minerals from each sample (n = 36). All analyses were performed on the JEOL JXA 8600 electron microprobe in the Department of Earth & Planetary Sciences, Johns Hopkins University. Calibration used multiple natural reference materials. Garnet traverses were run at 15 keV and 40 nA and used a 1-μm spot size at 1-μm centers and 30-s on-peak and 10-s background counting times. All other analyses were run at 15 keV and 20 nA and used a 5-μm spot size and 30-s on-peak and 15-s background counting times.

Results for the radial garnet traverses are provided in Fig. 1. Compositions of typical examples of minerals from CA13-01 and CA13-05A are provided in Tables 1 and 2. The subsequent section discusses mineral chemical variability and zoning. All quantitative electron microprobe results are provided in the Supplementary Materials.

Solid solution, mineral zoning, and Mn sources

Quantitative analyses demonstrate variability in composition for all minerals analyzed. Zoning in individual minerals can capture the full range of compositional variation observed for omphacite and zoisite in CA13-01 and hornblende and zoisite in CA13-05A. Amphiboles from CA13-01 are glaucophane, with Na/(Na + Ca) ≈ 94% (Fig. 7A). One population of amphibole in CA13-05A has similar glaucophane chemistry, whereas the other is a hornblende, with composition between actinolite and pargasite (Fig. 7A). Clinopyroxene in CA13-01 is omphacite, with 39 to 53 mole percent (mol %) jadeite (Fig. 7B). Chlorite in CA13-05A varies in composition, with Fe/(Fe + Mg) in the range 37 to 45% and Si increasing with Fe (Fig. 7C). White mica in CA13-01 also varies in composition, potentially defining two (phengitic) compositional arrays between celadonite and muscovite/paragonite (Fig. 7D). Phengite in CA13-01 has a Si content of 3.34 to 3.54 per formula unit.

The compositional arrays and populations of Fig. 7 are reflected in BSE zoning in amphibole and omphacite. In addition, zoisite has fine-scale, oscillatory BSE zoning (Fig. 8). The zoning principally relates to Fe^{3+} and Al substitution in the epidote-zoisite solid solution (Fig. 8 and Tables 1 and 2) but also maps with Mn content, particularly in CA13-05A (Fig. 8). Complementary Mn zoning in zoisite to that observed in garnet (see Results) suggests that zoisite growth may have partially balanced garnet dissolution (and vice versa). This observation is consistent with parallelism of modal garnet and zoisite contours (Fig. 9). Garnet breakdown in the presence of H_2O produces zoisite only if other reactants are able to balance the remaining chemistry.

Table 1. Stoichiometric mineral compositions for CA13-01, based on assumed number of oxygen atoms shown. Note that Fe in zoisite was assumed to be 100% Fe^{3+} and Fe in all other minerals was assumed to be 100% Fe^{2+}. Gln, glaucophane; Omph, omphacite; Phe, phengite; Zo, zoisite.

	CA13-01				
	Gln	Omph	Phe	Zo 1	Zo 2
Si	7.99	2.02	3.49	2.91	2.92
Ti	—	—	0.01	0.01	—
Al	1.69	0.36	1.97	2.41	2.25
Cr	—	—	—	—	—
Fe	1.15	0.22	0.19	0.50	0.62
Mn	—	—	—	—	0.01
Mg	2.21	0.44	0.39	0.01	—
Ca	0.15	0.51	—	1.79	1.72
Na	1.87	0.46	0.03	—	—
K	—	—	0.87	—	—
O	23	6	11	12.5	12.5
Al/(Al + Si)	0.17	0.15	0.36	0.45	0.44
Fe/(Fe + Al)	0.41	0.38	0.09	0.17	0.21
Fe/(Fe + Mg)	0.34	0.34	0.33	—	—
Na/(Na + Ca)	0.93	0.48	—	—	—
Na/(Na + K)	—	—	0.04	—	—
Total oxides (wt %)	97.5	100.6	94.5	96.3	97.6

Table 2. Stoichiometric mineral compositions for CA13-05A, based on assumed number of oxygen atoms shown. Note that Fe in zoisite was assumed to be 100% Fe^{3+} and Fe in all other minerals was assumed to be 100% Fe^{2+}. Hbl, hornblende; Gln, glaucophane; Chl, chlorite; Aln, allanite.

	CA13-05A						
	Hbl 1	Hbl 2	Gln	Chl	Zo 1	Zo 2	Aln
Si	7.29	6.92	7.85	2.97	2.91	2.85	2.94
Ti	0.02	0.03	0.01	0.01	0.01	0.06	0.01
Al	1.24	1.91	1.77	2.32	2.41	2.09	2.01
Cr	—	—	—	—	—	—	—
Fe	1.56	1.57	1.30	1.84	0.51	0.73	0.87
Mn	0.02	0.01	0.01	0.02	0.01	0.02	0.02
Mg	3.00	2.67	2.21	2.68	—	—	—
Ca	1.50	1.47	0.12	—	1.77	1.70	1.40
Na	0.82	0.93	1.98	—	—	—	—
K	0.04	0.08	—	0.01	—	—	—
O	23	23	23	14	12.5	12.5	12.5
Al/(Al + Si)	0.15	0.22	0.18	0.44	0.45	0.42	0.41
Fe/(Fe + Al)	0.56	0.45	0.42	0.44	0.17	0.26	0.30
Fe/(Fe + Mg)	0.34	0.37	0.37	0.41	—	—	—
Na/(Na + Ca)	0.35	0.39	0.94	—	—	—	—
Na/(Na + K)	0.95	0.92	—	—	—	—	—
Total oxides (wt %)	97.1	98.9	97.1	86.1	96.7	97.2	81.0

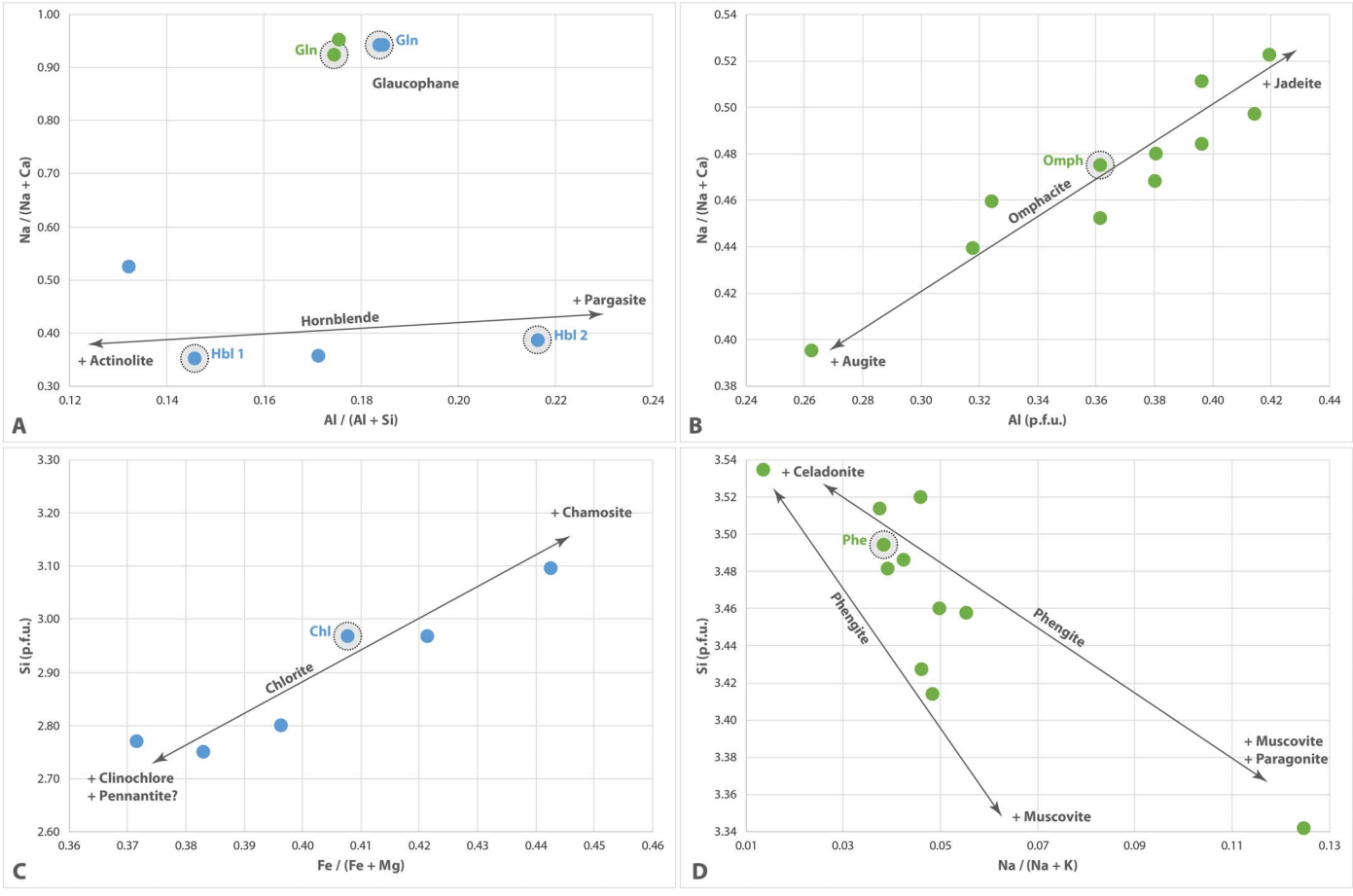

Fig. 7. Mineral composition plots. Plots showing solid solution for (**A**) amphibole, (**B**) clinopyroxene, (**C**) chlorite, and (**D**) white mica. Green data are for CA13-01, and blue data are for CA13-05A. Circled points are those whose geochemistry is given in Tables 1 and 2. p.f.u., per formula unit.

Garnet growth-dissolution reactions that mark *P* pulses (seismic loading-rupture cycles) may have involved garnet, jadeite, quartz, and H_2O to yield Na amphibole and zoisite (and vice versa) in CA13-05C, and garnet, Na amphibole, and H_2O to yield Na-Ca amphibole and zoisite (and vice versa) in CA13-01.

The predicted garnet growth–to–zoisite dissolution ratio for an isothermal, 250-MPa *P* pulse starting at $T = 570°C$ and $P = 1.55$ GPa is greater for CA13-01 (5:1.25) than for CA13-05A (9:4) (Fig. 9). The Mn-in-garnet–to–Mn-in-zoisite ratio is also greater for CA13-01 (approximately 1.0:0.1) than for CA13-05A (approximately 0.5:0.2). Hornblende, a product of garnet breakdown in CA13-05A, has up to 0.11 weight % (wt %) Mn. More accommodating hosts for Mn liberated during breakdown of garnet in CA13-05A may account for limited Mn back diffusion during garnet dissolution in CA13-05A (relative to CA13-01) and thus development of core-side rather than rim-side zoning in those garnets (see Fig. 2).

Whole-rock geochemistry and thermodynamic modeling method and results

Whole-rock geochemistry

Approximately 20 g of fresh and representative material from each of CA13-01 and CA13-05A was ground to powder in a tungsten carbide ring-and-puck mill. Lithium borate–fused glass beads were prepared for analysis with a sample (powder)-to-flux ratio of 1:5. Whole-rock geochemical analyses for major elements were performed on the PANalytical Axios Advanced x-ray fluorescence (XRF) spectrometer in the Department of Geology, University of Leicester. Results from the XRF work are provided in Table 3.

Perple_X thermodynamic modeling of metamorphic phase equilibria

Thermodynamic modeling of metamorphic phase equilibria was performed in the MnNCKFMASHT system using the whole-rock compositions in Table 3. Whole-rock compositions were considered in preference to porphyroblast-subtracted compositions as the modeling was performed to interrogate sensitivity of garnet content (and growth or dissolution) to changes in *P-T*; a highly responsive, porphyroblast-involved system was assumed. For each model, the rock was considered saturated in H_2O (set to 10 wt %), and Fe determined from XRF was recalculated to 100% ferrous (FeO); the only mineral in the rock with significant Fe^{3+} is epidote and that accounts for only a limited proportion of the zoisite (see Fig. 8). Modeling used version 6.6.6 of the Perple_X program (*66*, *67*) and the 2004 update of the thermodynamic data set of Holland and Powell (*68*). Solution models used for the modeling (and references) are provided in the Supplementary Materials. Modeling was performed in the following ranges: $T = 525°$ to 625°C and $P = 1.4$ to 2.4 GPa for CA13-01 and $T = 525°$ to 625°C and $P = 1.2$ to 2.2 GPa for CA13-05A. Figure 9 shows metamorphic assemblage diagrams for both samples, with modal abundance contours for both

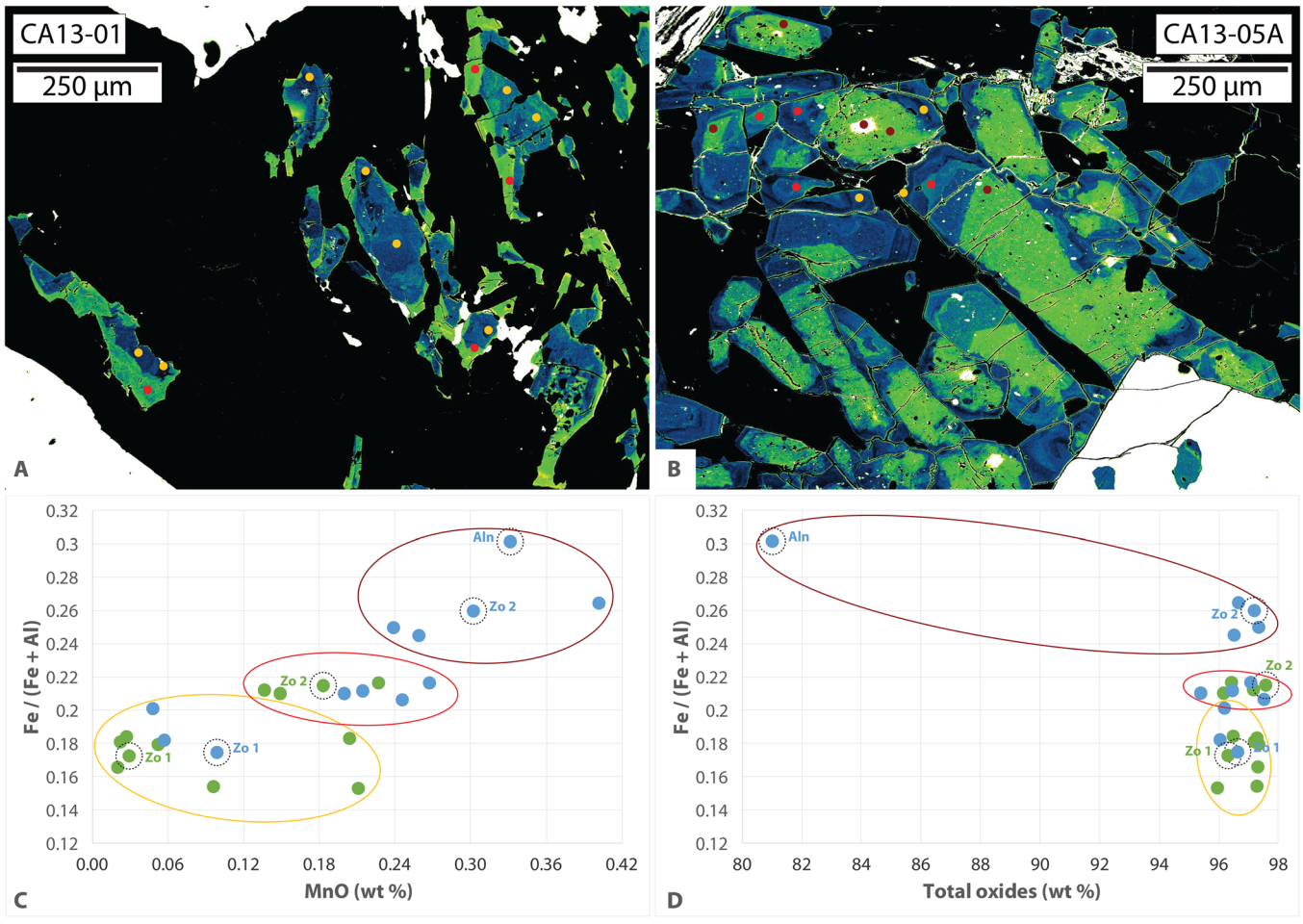

Fig. 8. Zoisite zoning and composition. (**A** and **B**) Color overlay BSE maps for zoisite in CA13-01 and CA13-05A, highlighting fine-scale oscillatory zoning. (**C**) Discrimination plot showing positive correlation between Fe/(Fe + Al) and MnO in zoisite. (**D**) Discrimination plot showing one analysis distinct from others on the basis of lower oxide totals: an allanite that contains a high proportion of trace elements not analyzed for. Green data are for CA13-01, and blue data are for CA13-05A. Yellow, red, and maroon groupings match the color of analysis spots and low to high BSE response, respectively, in the maps. Spots on maps are three times larger than actual analyses.

garnet and zoisite (Fig. 9, A and B) and Mg garnet (pyrope) and Mn garnet (spessartine) (Fig. 9, C and D) overlain.

Raman thermobarometry method and results

Raman spectroscopy was performed on quartz inclusions in garnet using a HORIBA Jobin Yvon LabRAM HR Raman microscope in the Department of Chemistry, Durham University. All analyses used an 1800 grid (1800 grooves mm^{-1} grating), centered at 470 cm^{-1}. For each quartz inclusion analysis, a 100× confocal objective lens was used to focus the 632.8-nm (red) HeNe laser to a spot size of 1 µm, centered in the inclusion. Quartz inclusions were inspected for exposure and/or cross-cutting cracks and analyzed in triplicate (three measurements in separate sessions). Precise peak positions were obtained by fitting Lorentzian curves to the nominal 464 cm^{-1} A1g-mode quartz Raman peak (for unknowns) using the software package Igor Pro. Curve fitting to the nominal 464 cm^{-1} A1g-mode peak in quartz used the portion of the spectrum 12 grid points on either side of the maximum intensity position, representing a total range of ~7.6 cm^{-1}.

Instrument drift due to internal temperature equilibration was corrected for by quasi-hourly (duplicate) measurement of a pure sulfur Raman spectroscopy standard. Analyses on sulfur standards used a 50× objective and the same 632.8-nm (red) HeNe laser, focused to the position within the homogeneous standard that produced maximum spectrum intensity. For the sulfur standard spectra, curve fitting to the nominal 384.1 cm^{-1} mode peak used the portion of the spectra eight grid points on either side of the maximum intensity position (total range of ~5.1 cm^{-1}), a Lorentzian form, and the software package Igor Pro. Drift in the position of the nominal 384.1 cm^{-1} sulfur peak during each Raman session was characterized by an equation of the form $[y = -A \exp(-t/b) + c]$, where y is the measured peak position minus the nominal 384.1 cm^{-1} value, t is the time since the first measurement of the session, A and b are shape constants, and c is a vertical shift constant. Values of A, b, and c for each session were calculated from a fit to the sulfur data for that session. Following correction for instrument drift at the time of measurement, unknowns were found to have an overall 2σ reproducibility of ±0.3 cm^{-1} for the peak position of the nominal 464 cm^{-1} A1g-mode quartz Raman peak, despite measurements being made on separate days (see Results and Fig. 3). Uncorrected spectra (with time stamps) for both quartz inclusions (unknowns) and sulfur standards are available at https://doi.org/10.7281/T1/SP6KO3.

Calculation of overgrowth P and T used the MATLAB QuiB Calc program of Ashley *et al.* (*69*), the quartz Raman calibration of Schmidt

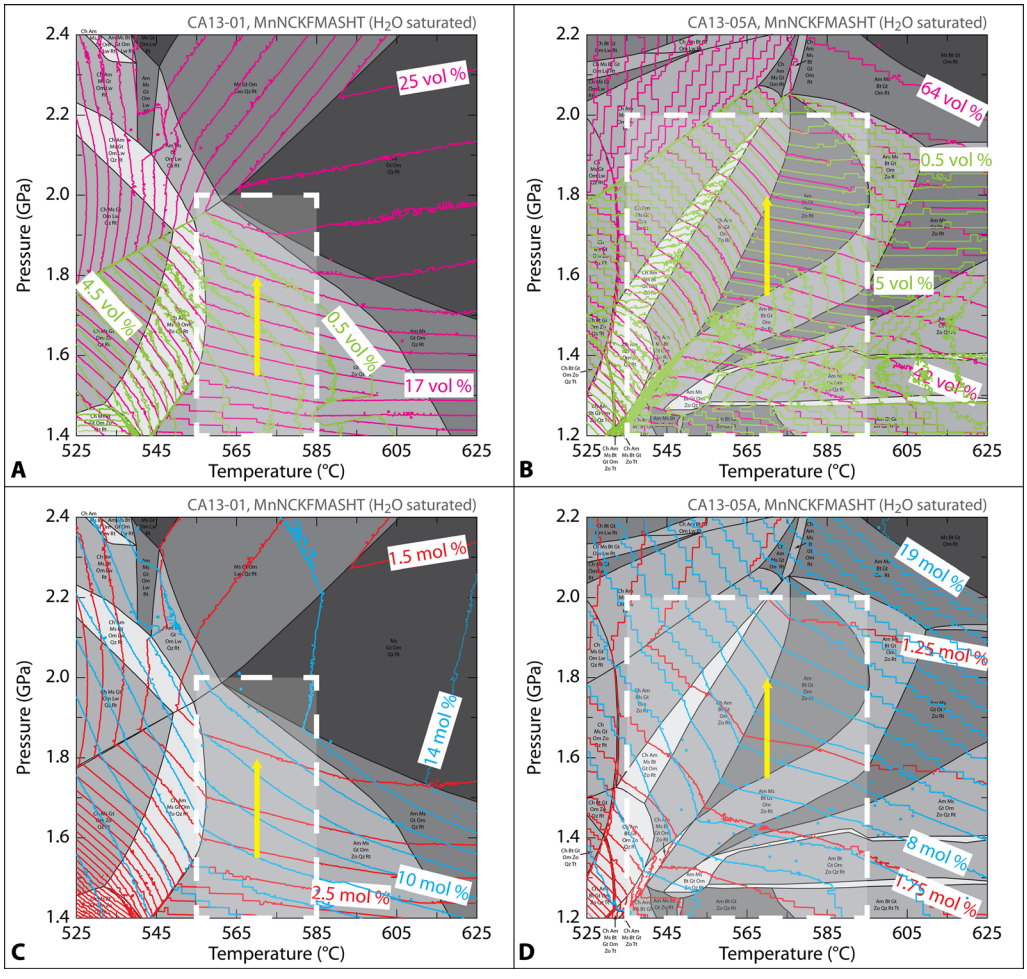

Fig. 9. Results of thermodynamic modeling. MnNCKFMASHT metamorphic assemblage diagrams for (**A** and **C**) CA13-01 and (**B** and **D**) CA13-05A. Phase assemblage fields and labels redrafted from the Perple_X output. White dashed box indicates approximate equilibrium *P-T* range of the peak-metamorphic assemblage in each rock. Green and pink contours in (A) and (B) are for modal zoisite and garnet, respectively; contour intervals of 0.5 volume % are used for zoisite, and contour intervals of 1 and 2 volume % are used for garnet in CA13-01 and CA13-05A, respectively. Note the significant congruence between zoisite and garnet contours, suggesting a metamorphic relationship between the phases (that is, the dissolution of one partially accommodates the growth of the other). The yellow arrow shows a 250-MPa isothermal *P* increase (starting at *T* = 570°C and *P* = 1.55 GPa), associated with an absolute gain of 5 volume % garnet and loss of 1.25 volume % zoisite for CA13-01 and an absolute gain of 9 volume % garnet and loss of 4 volume % zoisite for CA13-05A. Blue and red contours in (C) and (D) are for proportion of Mg garnet (pyrope) and Mn garnet (spessartine), respectively; contour intervals of 1 mol % are used for pyrope, and contour intervals of 0.25 mol % are used for spessartine.

Table 3. Whole-rock geochemistry determined by XRF (values in wt %). LOI, loss on ignition.

	SiO_2	TiO_2	Al_2O_3	Fe_2O_3	MnO	MgO	CaO	Na_2O	K_2O	P_2O_5	SO_3	LOI	Total
CA13-01	48.09	1.53	15.78	9.90	0.19	5.38	10.74	3.49	1.54	0.12	<0.002	1.26	98.02
CA13-05A	40.85	2.84	16.43	17.23	0.35	6.36	12.53	1.11	0.13	0.10	0.112	1.28	99.32

and Ziemann (*40*), mineral properties compiled in Holland and Powell (*42*), and the elastic model of Guiraud and Powell (*41*). Properties of garnet were calculated by linear interpolation between almandine, grossular, pyrope, and spessartine using respective molar ratios of 59:26:11:4 for CA13-01 and 56:28:15:1 for CA13-05A. These garnet compositions match microprobe-determined rim compositions for the garnets (see Fig. 1). For the same Raman shifts, the elastic model of Zhang (*70*) yields *P* estimates that are systematically higher by 100 to 200 MPa.

Synchrotron FTIR method and results

Microanalyses made at the Diamond Light Source were performed in transmission mode, with a spectral resolution of 16 cm^{-1} and a phase resolution of 128, using a 700 to 3200 cm^{-1} window. Analyses used a

36× objective and a 10 μm × 10 μm square slit size defining the detected area at the sample. Each spectrum was produced from 3000 scans, and backgrounds were collected before each traverse. Four traverses were run radially across the zoning at the garnet edge, using 10-μm centers (n = 39 for CA13-01 G1T2, n = 35 for CA13-01 G2T1, n = 76 for CA13-05A G1T1, and n = 46 for CA13-05A G2T1). Microanalyses made at the Australian Synchrotron were also performed in transmission mode, with a spectral resolution of 16 cm^{-1} and a phase resolution of 128, using a 700 to 3200 cm^{-1} window. Analyses again used a 36× objective but a circular spot size of 11.6 μm. Each spectrum was produced from 512 scans, and backgrounds were collected before each map. The 2D maps approximated 1D radial traverses, forming elongate grids with the following dimensions: 6 × 44 (n = 264) for CA13-01 G1T3, 5 × 39 (n = 195) for CA13-01 G2T2, 6 × 45 (n = 270) for CA13-01 G3T1, 6 × 81 (n = 486) for CA13-05A G1T2, and 6 × 48 (n = 288) for CA13-05A G2T2. All line maps used 12-μm centers in the "circumferential" direction and 6-μm centers (approximate 2× oversampling) in the radial direction. CA13-01 garnet 2, map G2T2, collected at the Australian Synchrotron, experienced irrecoverable issues with background correction.

In total, analyses were performed in transmission mode on three garnets from a clean, ~225-μm-thick wafer of sample CA13-01 and two garnets from a clean, ~280-μm-thick wafer of sample CA13-05A. Relative OH and H_2O contents were calculated from the integrated intensity of the background-subtracted spectra in the 3520 to 3620 cm^{-1} and 3350 to 3450 cm^{-1} mid-IR regions, respectively. Integrated intensity calculations were performed with the OPUS software package using a linear integration baseline. Processed data for the integrated intensities of OH and H_2O in the five garnets analyzed by synchrotron FTIR spectroscopy are provided in Fig. 4. Raw data (as OPUS files) for all synchrotron FTIR analyses are available at https://doi.org/10.7281/T1/SP6KO3.

SUPPLEMENTARY MATERIALS

Supplementary material for this article is available at http://advances.sciencemag.org/cgi/content/full/4/3/eaaq0234/DC1

fig. S1. Color overlay x-ray count maps for major divalent elements in Garnet 1.1 from CA13-01.
fig. S2. Color overlay x-ray count maps for major divalent elements in Garnet 1.4 from CA13-01.
fig. S3. Color overlay x-ray count maps for major divalent elements in Garnet 1.5 from CA13-01.
fig. S4. Color overlay x-ray count maps for major divalent elements in Garnet 1.6 from CA13-01.
fig. S5. Color overlay x-ray count maps for major divalent elements in Garnet 2.1 from CA13-01.
fig. S6. Color overlay x-ray count maps for major divalent elements in Garnet 2.2 from CA13-01.
fig. S7. Color overlay x-ray count maps for major divalent elements in Garnet 2.3 from CA13-01.
fig. S8. Color overlay x-ray count maps for major divalent elements in Garnet 1.2 from CA13-05A.
fig. S9. Color overlay x-ray count maps for major divalent elements in Garnet 1.4 from CA13-05A.
fig. S10. Color overlay x-ray count maps for major divalent elements in Garnet 1.7 from CA13-05A.
fig. S11. Color overlay x-ray count maps for major divalent elements in Garnet 1.8 from CA13-05A.
fig. S12. Color overlay x-ray count maps for major divalent elements in Garnet 2.1 from CA13-05A.
fig. S13. Color overlay x-ray count maps for major divalent elements in Garnet 2.2 from CA13-05A.
fig. S14. Color overlay x-ray count maps for Mg in garnets from CA13-01 and CA13-05A.
fig. S15. Color overlay x-ray count maps for Mn in garnets from CA13-01 and CA13-05A.
fig. S16. Blowups of regions indicated by white rectangles in (top row) fig. S14 and (bottom row) fig. S15.
Excel file
References (*71*–*83*)

REFERENCES AND NOTES

1. J. Nakajima, A. Hasegawa, S. Kita, Seismic evidence for reactivation of a buried hydrated fault in the Pacific slab by the 2011 M9.0 Tohoku earthquake. *Geophys. Res. Lett.* **38**, L00G06 (2011).
2. C. Spandler, T. Pettke, D. Rubatto, Internal and external fluid sources for eclogite-facies veins in the Monviso meta-ophiolite, western Alps: Implications for fluid flow in subduction zones. *J. Petrol.* **52**, 1207–1236 (2011).
3. J. H. Davies, The role of hydraulic fractures and intermediate-depth earthquakes in generating subduction-zone magmatism. *Nature* **398**, 142–145 (1999).
4. T. John, N. Gussone, Y. Y. Podladchikov, G. E. Bebout, R. Dohmen, R. Halama, R. Klemd, T. Magna, H.-M. Seitz, Volcanic arcs fed by rapid pulsed fluid flow through subducting slabs. *Nat. Geosci.* **5**, 489–492 (2012).
5. C. Frohlich, The nature of deep-focus earthquakes. *Annu. Rev. Earth Planet. Sci.* **17**, 227–254 (1989).
6. S. Kirby, E. R. Engdahl, R. Denlinger, Intermediate-depth intraslab earthquakes and arc volcanism as physical expressions of crustal and uppermost mantle metamorphism in subducting slabs, in *Subduction: Top to Bottom*, G. E. Bebout, D. W. Scholl, S. H. Kirby, J. P. Platt, Eds. (Geophysical Monograph Series, American Geophysical Union, 1996), vol. 96, pp. 195–214.
7. G. A. Abers, P. E. van Keken, E. A. Kneller, A. Ferris, J. C. Stachnik, The thermal structure of subduction zones constrained by seismic imaging: Implications for slab dehydration and wedge flow. *Earth Planet. Sci. Lett.* **241**, 387–397 (2006).
8. H. W. Green II, W.-P. Chen, M. R. Brudzinski, Seismic evidence of negligible water carried below 400-km depth in subducting lithosphere. *Nature* **467**, 828–831 (2010).
9. H. W. Green II, H. Houston, The mechanics of deep earthquakes. *Annu. Rev. Earth Planet. Sci.* **23**, 169–213 (1995).
10. B. R. Hacker, S. M. Peacock, G. A. Abers, S. D. Holloway, Subduction factory 2. Are intermediate-depth earthquakes in subducting slabs linked to metamorphic dehydration reactions? *J. Geophys. Res.* **108**, 2030 (2003).
11. L. A. Preston, K. C. Creager, R. S. Crosson, T. M. Brocher, A. M. Trehu, Intraslab earthquakes: Dehydration of the cascadia slab. *Science* **302**, 1197–1200 (2003).
12. H. Jung, H. W. Green II, L. F. Dobrzhinetskaya, Intermediate-depth earthquake faulting by dehydration embrittlement with negative volume change. *Nature* **428**, 545–549 (2004).
13. J. Nakajima, N. Uchida, T. Shiina, A. Hasegawa, B. R. Hacker, S. H. Kirby, Intermediate-depth earthquakes facilitated by eclogitization-related stresses. *Geology* **41**, 659–662 (2013).
14. A. Schubnel, F. Brunet, N. Hilairet, J. Gasc, Y. Wang, H. W. Green II, Deep-focus earthquake analogs recorded at high pressure and temperature in the laboratory. *Science* **341**, 1377–1380 (2013).
15. J. Adams, Paleoseismicity of the Cascadia subduction zone: Evidence from turbidites off the Oregon–Washington margin. *Tectonics* **9**, 569–583 (1990).
16. C. Goldfinger, C. H. Nelson, J. E. Johnson; The Shipboard Scientific Party, Holocene earthquake records from the Cascadia subduction zone and northern San Andreas fault based on precise dating of offshore turbidites. *Annu. Rev. Earth Planet. Sci.* **31**, 555–577 (2003).
17. F. Nanayama, K. Satake, R. Furukawa, K. Shimokawa, B. F. Atwater, K. Shigeno, S. Yamaki, Unusually large earthquakes inferred from tsunami deposits along the Kuril trench. *Nature* **424**, 660–663 (2003).
18. M. Cisternas, B. F. Atwater, F. Torrejón, Y. Sawai, G. Machuca, M. Lagos, A. Eipert, C. Youlton, I. Salgado, T. Kamataki, M. Shishikura, C. P. Rajendran, J. K. Malik, Y. Rizal, M. Husni, Predecessors of the giant 1960 Chile earthquake. *Nature* **437**, 404–407 (2005).
19. K. Monecke, W. Finger, D. Klarer, W. Kongko, B. G. McAdoo, A. L. Moore, S. U. Sudrajat, A 1,000-year sediment record of tsunami recurrence in northern Sumatra. *Nature* **455**, 1232–1234 (2008).
20. E. Gràcia, A. Vizcaino, C. Escutia, A. Asioli, Á. Rodés, R. Pallàs, J. Garcia-Orellana, S. Lebreiro, C. Goldfinger, Holocene earthquake record offshore Portugal (SW Iberia): Testing turbidite paleoseismology in a slow-convergence margin. *Quat. Sci. Rev.* **29**, 1156–1172 (2010).
21. F. W. Taylor, R. L. Edwards, G. J. Wasserburg, C. Frohlich, Seismic recurrence intervals and timing of aseismic subduction inferred from emerged corals and reefs of the Central Vanuatu (New Hebrides) frontal arc. *J. Geophys. Res.* **95**, 393–408 (1990).
22. A. R. Nelson, I. Shennan, A. J. Long, Identifying coseismic subsidence in tidal-wetland stratigraphic sequences at the Cascadia subduction zone of western North America. *J. Geophys. Res.* **101**, 6115–6135 (1996).
23. H. Austrheim, T. M. Boundy, Pseudotachylytes generated during seismic faulting and eclogitization of the deep crust. *Science* **265**, 82–83 (1994).
24. T. John, V. Schenk, Interrelations between intermediate-depth earthquakes and fluid flow within subducting oceanic plates: Constraints from eclogite facies pseudotachylytes. *Geology* **34**, 557–560 (2006).

25. S. Angiboust, P. Agard, P. Yamato, H. Raimbourg, Eclogite breccias in a subducted ophiolite: A record of intermediate-depth earthquakes? *Geology* **40**, 707–710 (2012).
26. M. G. Bjørnerud, H. Austrheim, M. G. Lund, Processes leading to eclogitization (densification) of subducted and tectonically buried crust. *J. Geophys. Res.* **107**, 2252 (2002).
27. H. Raimbourg, B. Goffé, L. Jolivet, Garnet reequilibration and growth in the eclogite facies and geodynamical evolution near peak metamorphic conditions. *Contrib. Mineral. Petrol.* **153**, 1–28 (2007).
28. A. Camacho, J. K. W. Lee, B. J. Hensen, J. Braun, Short-lived orogenic cycles and the eclogitization of cold crust by spasmodic hot fluids. *Nature* **435**, 1191–1196 (2005).
29. B. Dragovic, L. M. Samanta, E. F. Baxter, J. Selverstone, Using garnet to constrain the duration and rate of water-releasing metamorphic reactions during subduction: An example from Sifnos, Greece. *Chem. Geol.* **314–317**, 9–22 (2012).
30. P. P. Dudley, Electron microprobe analyses of garnet in glaucophane schists and associated eclogites. *Am. Mineral.* **54**, 1139–1150 (1969).
31. A. García-Casco, R. L. Torres-Roldán, G. Millán, P. Monié, J. Schneider, Oscillatory zoning in eclogitic garnet and amphibole, Northern Serpentinite Melange, Cuba: A record of tectonic instability during subduction?. *J. Metam. Geol.* **20**, 581–598 (2002).
32. P. B. Davis, D. L. Whitney, Petrogenesis of lawsonite and epidote eclogite and blueschist, Sivrihisar Massif, Turkey. *J. Metam. Geol.* **24**, 823–849 (2006).
33. T. Tsujimori, K. Matsumoto, J. Wakabayashi, J. G. Liou, Franciscan eclogite revisited: Reevaluation of the *P–T* evolution of tectonic blocks from Tiburon Peninsula, California, U.S.A. *Mineral. Petrol.* **88**, 243–267 (2006).
34. F. Z. Page, L. S. Armstrong, E. J. Essene, S. B. Mukasa, Prograde and retrograde history of the Junction school eclogite, California, and an evaluation of garnet–phengite–clinopyroxene thermobarometry. *Contrib. Mineral. Petrol.* **153**, 533–555 (2007).
35. M. F. Kabir, A. Takasu, Evidence for multiple burial–partial exhumation cycles from the Onodani eclogites in the Sambagawa metamorphic belt, central Shikoku, Japan. *J. Metam. Geol.* **28**, 873–893 (2010).
36. M. Meyer, R. Klemd, T. John, J. Gao, M. Menneken, An (in-)coherent metamorphic evolution of high-*P* eclogites and their host rocks in the Chinese southwest Tianshan? *J. Metam. Geol.* **34**, 121–146 (2016).
37. T. Tsujimori, V. B. Sisson, J. G. Liou, G. E. Harlow, S. S. Sorensen, Petrologic characterization of Guatemalan lawsonite eclogite: Eclogitization of subducted oceanic crust in a cold subduction zone, in *Ultrahigh Pressure Metamorphism: Deep Continental Subduction*, B. R. Hacker, W. C. McClelland, J. G. Liou, Eds. (Geological Society of America Special Papers, 2006), vol. 403, pp. 147–168.
38. M. J. Kohn, "Thermoba-Raman-try": Calibration of spectroscopic barometers and thermometers for mineral inclusions. *Earth Planet. Sci. Lett.* **388**, 187–196 (2014).
39. K. T. Ashley, M. Steele-MacInnis, R. J. Bodnar, R. S. Darling, Quartz-in-garnet inclusion barometry under fire: Reducing uncertainty from model estimates. *Geology* **44**, 699–702 (2016).
40. C. Schmidt, M. A. Ziemann, In-situ Raman spectroscopy of quartz: A pressure sensor for hydrothermal diamond-anvil cell experiments at elevated temperatures. *Am. Mineral.* **85**, 1725–1734 (2000).
41. M. Guiraud, R. Powell, *P–V–T* relationships and mineral equilibria in inclusions in minerals. *Earth Planet. Sci. Lett.* **244**, 683–694 (2006).
42. T. J. B. Holland, R. Powell, An improved and extended internally consistent thermodynamic dataset for phases of petrological interest, involving a new equation of state for solids. *J. Metam. Geol.* **29**, 333–383 (2011).
43. R. Lu, H. Keppler, Water solubility in pyrope to 100 kbar. *Contrib. Mineral. Petrol.* **129**, 35–42 (1997).
44. A. C. Withers, B. J. Wood, M. R. Carroll, The OH content of pyrope at high pressure. *Chem. Geol.* **147**, 161–171 (1998).
45. F. Z. Page, E. J. Essene, S. B. Mukasa, J. W. Valley, A garnet–zircon oxygen isotope record of subduction and exhumation fluids from the Franciscan Complex, California. *J. Petrol.* **55**, 103–131 (2014).
46. E. J. Krogh, C. W. Oh, J. G. Liou, Polyphase and anticlockwise *P-T* evolution for Franciscan eclogites and blueschists from Jenner, California, USA. *J. Metam. Geol.* **12**, 121–134 (1994).
47. J. Wakabayashi, Counterclockwise P-T-t paths from amphibolites, Franciscan Complex, California: Relics from the early stages of subduction zone metamorphism. *J. Geol.* **98**, 657–680 (1990).
48. R. Anczkiewicz, J. P. Platt, M. F. Thirlwall, J. Wakabayashi, Franciscan subduction off to a slow start: Evidence from high-precision Lu–Hf garnet ages on high-grade blocks. *Earth Planet. Sci. Lett.* **225**, 147–161 (2004).
49. X. Chu, J. J. Ague, Analysis of experimental data on divalent cation diffusion kinetics in aluminosilicate garnets with application to timescales of peak Barrovian metamorphism, Scotland. *Contrib. Mineral. Petrol.* **170**, 25 (2015).
50. S. Chakraborty, J. Ganguly, Cation diffusion in aluminosilicate garnets: Experimental determination in spessartine–almandine diffusion couples, evaluation of effective binary diffusion coefficients, and applications. *Contrib. Mineral. Petrol.* **111**, 74–86 (1992).
51. W. D. Carlson, Rates of Fe, Mg, Mn, and Ca diffusion in garnet. *Am. Mineral.* **91**, 1–11 (2006).
52. E. M. Syracuse, G. A. Abers, Global compilation of variations in slab depth beneath arc volcanoes and implications. *Geochem. Geophys. Geosyst.* **7**, Q05017 (2006).
53. M. Beltrando, J. Hermann, G. S. Lister, R. Compagnoni, On the evolution of orogens: Pressure cycles and deformation mode switches. *Earth Planet. Sci. Lett.* **256**, 372–388 (2007).
54. D. Rubatto, D. Regis, J. Hermann, K. Boston, M. Engi, M. Beltrando, S. R. B. McAlpine, Yo-yo subduction recorded by accessory minerals in the Italian Western Alps. *Nat. Geosci.* **4**, 338–342 (2011).
55. G. S. Lister, M. A. Forster, White mica $^{40}Ar/^{39}Ar$ age spectra and the timing of multiple episodes of high-*P* metamorphic mineral growth in the Cycladic eclogite–blueschist belt, Syros, Aegean Sea, Greece. *J. Metam. Geol.* **34**, 401–421 (2016).
56. J. Wakabayashi, Subducted sedimentary serpentinite mélanges: Record of multiple burial–exhumation cycles and subduction erosion. *Tectonophysics* **568–569**, 230–247 (2012).
57. T. Gerya, B. Stöckhert, Two-dimensional numerical modelling of tectonic and metamorphic histories at active continental margins. *Int. J. Earth Sci.* **95**, 250–274 (2006).
58. T. V. Gerya, B. Stöckhert, A. L. Perchuk, Exhumation of high-pressure metamorphic rocks in a subduction channel: A numerical simulation. *Tectonics* **21**, 1056 (2002).
59. I. F. Blanco-Quintero, A. García-Casco, T. V. Gerya, Tectonic blocks in serpentinite mélange (eastern Cuba) reveal large-scale convective flow of the subduction channel. *Geology* **39**, 79–82 (2011).
60. J.-L. Li, R. Klemd, J. Gao, T. John, Poly-cyclic metamorphic evolution of eclogite: Evidence for multistage burial–exhumation cycling in a subduction channel. *J. Petrol.* **57**, 119–146 (2016).
61. F. Brenguier, M. Campillo, T. Takeda, Y. Aoki, N. M. Shapiro, X. Briand, K. Emoto, H. Miyake, Mapping pressurized volcanic fluids from induced crustal seismic velocity drops. *Science* **345**, 80–82 (2014).
62. E. J. Chaves, S. Y. Schwartz, Monitoring transient changes within overpressured regions of subduction zones using ambient seismic noise. *Sci. Adv.* **2**, e1501289 (2016).
63. J. C. Vrijmoed, Y. Y. Podladchikov, T. B. Andersen, E. H. Hartz, An alternative model for ultra-high pressure in the Svartberget Fe–Ti garnet-peridotite, Western Gneiss Region, Norway. *Eur. J. Mineral.* **21**, 1119–1133 (2009).
64. J. A. Padrón-Navarta, V. L. Sánchez-Vizcaíno, C. J. Garrido, M. T. Gómez-Pugnaire, Metamorphic record of high-pressure dehydration of antigorite serpentinite to chlorite harzburgite in a subduction setting (Cerro del Almirez, Nevado–Filábride complex, southern Spain). *J. Petrol.* **52**, 2047–2078 (2011).
65. P. I. Nabelek, Hydrofracturing of sediment and hydrated MORB's during subduction of ocean crust, American Geophysical Union Fall Meeting, Moscone South, 16 December 2015.
66. J. A. D. Connolly, Computation of phase equilibria by linear programming: A tool for geodynamic modeling and its application to subduction zone decarbonation. *Earth Planet. Sci. Lett.* **236**, 524–541 (2005).
67. J. A. D. Connolly, The geodynamic equation of state: What and how. *Geochem. Geophys. Geosyst.* **10**, Q10014 (2009).
68. T. J. B. Holland, R. Powell, An internally consistent thermodynamic data set for phases of petrological interest. *J. Metam. Geol.* **16**, 309–343 (1998).
69. K. T. Ashley, M. Steele-MacInnis, M. J. Caddick, *QuIB CalC*: A MATLAB® script for geobarometry based on Raman spectroscopy and elastic modeling of quartz inclusions in garnet. *Comput. Geosci.* **66**, 155–157 (2014).
70. Y. Zhang, Mechanical and phase equilibria in inclusion–host systems. *Earth Planet. Sci. Lett.* **157**, 209–222 (1998).
71. C. J. Wei, R. Powell, Phase relations in high-pressure metapelites in the system KFMASH (K_2O–FeO–MgO–Al_2O_3–SiO_2–H_2O) with application to natural rocks. *Contrib. Mineral. Petrol.* **145**, 301–315 (2003).
72. R. W. White, R. Powell, G. N. Phillips, A mineral equilibria study of the hydrothermal alteration in mafic greenschist facies rocks at Kalgoorlie, Western Australia. *J. Metam. Geol.* **21**, 455–468 (2003).
73. R. Powell, T. J. B. Holland, Relating formulations of the thermodynamics of mineral solid solutions: Activity modeling of pyroxenes, amphiboles, and micas. *Am. Mineral.* **84**, 1–14 (1999).
74. R. W. White, R. Powell, T. J. B. Holland, B. A. Worley, The effect of TiO_2 and Fe_2O_3 on metapelitic assemblages at greenschist and amphibolite facies conditions: Mineral equilibria calculations in the system K_2O–FeO–MgO–Al_2O_3–SiO_2–H_2O–TiO_2–Fe_2O_3. *J. Metam. Geol.* **18**, 497–511 (2000).
75. T. J. B. Holland, J. Baker, R. Powell, Mixing properties and activity–composition relationships of chlorites in the system MgO–FeO–Al_2O_3–SiO_2–H_2O. *Eur. J. Mineral.* **10**, 395–406 (1998).
76. E. Green, T. J. B. Holland, R. Powell, An order-disorder model for omphacitic pyroxenes in the system jadeite-diopside-hedenbergite-acmite, with application to eclogitic rocks. *Am. Mineral.* **92**, 1181–1189 (2007).

77. J. F. A. Diener, R. Powell, Revised activity–composition models for clinopyroxene and amphibole. *J. Metam. Geol.* **30**, 131–142 (2012).
78. M. L. Fuhrman, D. H. Lindsley, Ternary-feldspar modeling and thermometry. *Am. Mineral.* **73**, 201–215 (1998).
79. J. A. D. Connolly, V. Trommsdorff, Petrogenetic grids for metacarbonate rocks: Pressure-temperature phase-diagram projection for mixed-volatile systems. *Contrib. Mineral. Petrol.* **108**, 93–105 (1991).
80. T. J. B. Holland, R. Powell, Calculation of phase relations involving haplogranitic melts using an internally consistent thermodynamic dataset. *J. Petrol.* **42**, 673–683 (2001).
81. R. W. White, R. Powell, T. J. B. Holland, Calculation of partial melting equilibria in the system Na_2O–CaO–K_2O–FeO–MgO–Al_2O_3–SiO_2–H_2O (NCKFMASH). *J. Metam. Geol.* **19**, 139–153 (2001).
82. R. Coggon, T. J. B. Holland, Mixing properties of phengitic micas and revised garnet–phengite thermobarometers. *J. Metam. Geol.* **20**, 683–696 (2002).
83. E. Auzanneau, M. W. Schmidt, D. Vielzeuf, J. A. D. Connolly, Titanium in phengite: A geobarometer for high temperature eclogites. *Contrib. Mineral. Petrol.* **159**, 1–24 (2010).

Acknowledgments: K. Livi provided technical assistance for electron microprobe work at Johns Hopkins University. K. Chamberlain, G. Cooper, and E. Finch helped with the synchrotron FTIR work. A. Beeby provided access to the Raman Spectroscopy Laboratory at Durham University. Discussions with M. Brown helped hone the proposed model for seismicity-driven metamorphism. The paper benefitted greatly from the comments of five anonymous reviewers. **Funding:** Funding for the work was awarded by the Australian-American Fulbright Commission (Fulbright Victoria Fellowship to D.R.V.) and Durham University and Marie Skłodowska-Curie actions of the European Union (International Junior Research Fellowship to D.R.V.). Microprobe mapping work was supported by the University of California, Santa Barbara and NSF EAR-1219942. Synchrotron FTIR work was supported by a Rapid Access beamtime award from the Diamond Light Source (#SM14590) and a Merit Access beamtime award from the Australian Synchrotron (#11167). **Author contributions:** D.R.V. initiated and led the study, with input from B.R.H. and M.B.A.; D.R.V. wrote the paper, also with significant input from B.R.H. and M.B.A.; G.G.E.S. designed and performed the garnet electron microprobe mapping work; M.J.T., C.S.K., and G.C. facilitated (and helped interpret results from) the synchrotron FTIR work; and A.R.D. helped collect and analyze the Raman data. **Competing interests:** The authors declare that they have no competing interests. **Data and materials availability:** All data needed to evaluate the conclusions in the paper are present in the paper, in the Supplementary Materials, and/or in the online data repository at https://doi.org/10.7281/T1/SP6KO3. Data may also be requested from D.R.V.

Submitted 21 September 2017
Accepted 7 February 2018
Published 21 March 2018
10.1126/sciadv.aaq0234

Citation: D. R. Viete, B. R. Hacker, M. B. Allen, G. G. E. Seward, M. J. Tobin, C. S. Kelley, G. Cinque, A. R. Duckworth, Metamorphic records of multiple seismic cycles during subduction. *Sci. Adv.* **4**, eaaq0234 (2018).

Metamorphic records of multiple seismic cycles during subduction

Daniel R. Viete, Bradley R. Hacker, Mark B. Allen, Gareth G. E. Seward, Mark J. Tobin, Chris S. Kelley, Gianfelice Cinque and Andrew R. Duckworth

Sci Adv **4** (3), eaaq0234.
DOI: 10.1126/sciadv.aaq0234